Mon. Not. R. Astron. Soc. **385,** 1576–1584 (2008) doi:10.1111/j.1365-2966.2008.12939.x

WASP-3b: a strongly irradiated transiting gas-giant planet

D. Pollacco,[1⋆] I. Skillen,[2] A. Collier Cameron,[3] B. Loeillet,[4] H. C. Stempels,[3] F. Bouchy,[5,6] N. P. Gibson,[1] L. Hebb,[3] G. Hébrard,[5] Y. C. Joshi,[1] I. McDonald,[7] B. Smalley,[7] A. M. S. Smith,[3] R. A. Street,[1,8] S. Udry,[9] R. G. West,[10] D. M. Wilson,[7] P. J. Wheatley,[11] S. Aigrain,[12] K. Alsubai,[3] C. R. Benn,[2] V. A. Bruce,[3] D. J. Christian,[1] W. I. Clarkson,[13,14] B. Enoch,[13] A. Evans,[7] A. Fitzsimmons,[1] C. A. Haswell,[13] C. Hellier,[7] S. Hickey,[2,15] S. T. Hodgkin,[12] K. Horne,[3] M. Hrudková,[2,16] J. Irwin,[12] S. R. Kane,[2,17] F. P. Keenan,[1] T. A. Lister,[3,7,8] P. Maxted,[7] M. Mayor,[9] C. Moutou,[4] A. J. Norton,[13] J. P. Osborne,[10] N. Parley,[13] F. Pont,[9] D. Queloz,[9] R. Ryans[1] and E. Simpson[1]

[1]*Astrophysics Research Centre, School of Mathematics & Physics, Queen's University, University Road, Belfast BT7 1NN*
[2]*Isaac Newton Group of Telescopes, Apartado de Correos 321, E-38700 Santa Cruz de la Palma, Tenerife, Spain*
[3]*School of Physics and Astronomy, University of St Andrews, North Haugh, St Andrews, Fife KY16 9SS*
[4]*Laboratoire d'Astrophysique de Marseille, BP 8, 13376 Marseille Cedex 12, France*
[5]*Institut d'Astrophysique de Paris, CNRS (UMR 7095) – Université Pierre & Marie Curie, 98bis bvd. Arago, 75014 Paris, France*
[6]*Observatoire de Haute-Provence, 04870 St Michel l'Observatoire, France*
[7]*Astrophysics Group, Keele University, Staffordshire ST5 5BG*
[8]*Las Cumbres Observatory, 6740 Cortona Dr Suite 102, Santa Barbara, CA 93117, USA*
[9]*Observatoire de Genéve, Université de Genéve, 51 Ch. des Maillettes, 1290 Sauverny, Switzerland*
[10]*Department of Physics and Astronomy, University of Leicester, Leicester LE1 7RH*
[11]*Department of Physics, University of Warwick, Coventry CV4 7AL*
[12]*Institute of Astronomy, University of Cambridge, Madingley Road, Cambridge CB3 0HA*
[13]*Department of Physics and Astronomy, The Open University, Milton Keynes MK7 6AA*
[14]*STScI, 3700 San Martin Drive, Baltimore, MD 21218, USA*
[15]*Centre for Astrophysics, Science & Technology Research Institute, University of Hertfordshire, Hatfield AL10 9AB*
[16]*Astronomical Institute, Charles University Prague, V Holesovickach 2, CZ-180 00 Praha, Czech Republic*
[17]*Department of Astronomy, University of Florida, 211 Bryant Space Science Center, Gainesville, FL 32611-2055, USA*

Accepted 2008 January 9. Received 2008 January 9; in original form 2007 October 16

ABSTRACT

We report the discovery of WASP-3b, the third transiting exoplanet to be discovered by the WASP and SOPHIE collaboration. WASP-3b transits its host star USNO-B1.0 1256−0285133 every 1.846 834 ± 0.000 002 d. Our high-precision radial velocity measurements present a variation with amplitude characteristic of a planetary-mass companion and in phase with the light curve. Adaptive optics imaging shows no evidence for nearby stellar companions, and line-bisector analysis excludes faint, unresolved binarity and stellar activity as the cause of the radial velocity variations. We make a preliminary spectroscopic analysis of the host star and find it to have $T_{\rm eff} = 6400 \pm 100$ K and log $g = 4.25 \pm 0.05$ which suggests it is most likely an unevolved main-sequence star of spectral type F7-8V. Our simultaneous modelling of the transit photometry and reflex motion of the host leads us to derive a mass of $1.76^{+0.08}_{-0.14}$ $M_{\rm J}$ and radius $1.31^{+0.07}_{-0.14}$ $R_{\rm J}$ for WASP-3b. The proximity and relative temperature of the host star suggests that WASP-3b is one of the hottest exoplanets known, and thus has the potential to place stringent constraints on exoplanet atmospheric models.

Key words: methods: data analysis – techniques: photometric – techniques: radial velocities – planetary systems.

⋆E-mail: d.pollacco@qub.ac.uk

1 INTRODUCTION

Since the discovery by Henry et al. (2000) and Charbonneau et al. (2000) of the first transiting exoplanet, HD209458b, a further 22 transiting systems have been announced (see http://www.inscience.ch/transits). Transiting exoplanets are highly prized because the transit geometry tightly constrains their orbital inclinations and radii, and when coupled with radial velocity (RV) information, allows their masses to be derived. The mass–radius relation for exoplanets allows us to probe their internal structure, since it is these parameters which are compared with models of planetary structure and evolution (e.g. Sato et al. 2005; Guillot et al. 2006). The limited numbers of transiting exoplanets studied so far show remarkable diversity in their physical parameters. For example, planets with masses $M \sim 1M_{\rm J}$ range in size from 0.8 to $1.5R_{\rm J}$ for reasons that still elude us, although several plausible explanations have been proposed (e.g. Gu, Bodenheimer & Lin 2004; Arras & Bildsten 2006; Burrows et al. 2007; Fortney, Marley & Barnes 2007). The discovery of transiting planets in greater numbers will allow us to further explore the mass–radius plane, and thereby constrain theories of planetary formation, migration and evolution.

The discovery of the first exoplanet around a solar type star, 51 Peg b, was by the RV method (Mayor & Queloz 1995), and this technique is responsible for the discovery of the vast majority of the known exoplanetary systems, including HD209458b. However, following the discovery of the transits of HD209458b (Charbonneau et al. 2000; Henry et al. 2000) it was widely believed that the multiplex advantage of wide-field photometric imaging could lead to this technique becoming the dominant method for detecting exoplanets. While it is true to say that, at least initially, photometric surveys have been slow to realize their expected detection rates (Horne 2003), recently this situation has begun to change with 14 new systems published in 2006–07 alone. This improved detection rate is largely due to the development of a better understanding of noise characteristics, especially the correlated noise inherent in such photometric surveys (e.g. Gaudi, Seager & Mallen-Ornelas 2005; Gaudi 2005; Pont, Zucker & Queloz 2006; Smith et al. 2006). Transiting planets now comprise approximately 10 per cent of the known exoplanets. Successful exoplanet photometric surveys include the Wide Angle Search for Planets (WASP) Project (Pollacco et al. 2006), the Hungarian Automatic Telescope (HAT) Network (Bakos et al. 2004), OGLE (Udalski et al. 2002), the Trans-Atlantic Exoplanet Survey (TrES) (Dunham et al. 2004; O'Donovan et al. 2006) and the XO group (McCullough et al. 2006). The WASP project has published two new systems in the last year: WASP-1b and WASP-2b (Collier Cameron et al. 2007a) and WASP-1b, in particular, has proved to be especially interesting, being well oversized compared to other planets for its mass.

In this paper the WASP and SOPHIE collaboration announce the discovery of a new, relatively high-mass, strongly irradiated gas-giant exoplanet, WASP-3b.

2 OBSERVATIONS AND DATA REDUCTION

2.1 SuperWASP-N photometry

The photometric observations used in this study are from the inaugural 2004 SuperWASP-N observing season, which ran from April to September of that year; this data set also led to the discovery of WASP-1b and WASP-2b. Briefly, in 2004 the SuperWASP-N instrument comprised four, and at times, five optical cameras, each consisting of a Canon 200 mm f/1.8 telephoto lens imaging on to a thermoelectrically cooled, science-grade 2048 × 2048 CCD camera (manufactured by e2v Technologies PLC). In this system, the CCD's 13.5 μm pixels project to an angular size of 14.2 arcsec. For the entirety of the 2004 season, while robotic operation was being commissioned, the instrument performance was supervised with an observer always in attendance, although data acquisition was fully automated. Data were shipped to the UK on a weekly basis and reduced at the home institutes of the WASP Consortium using a dedicated, purpose-built pipeline, and the results ingested into the project data base at the University of Leicester. The entire project infrastructure is described in detail by Pollacco et al. (2006) along with the deployment of a further facility, WASP-S, at the South African Astronomical Observatory. SuperWASP-N now runs completely robotically, and data are transferred to the UK in near real time over the Internet.

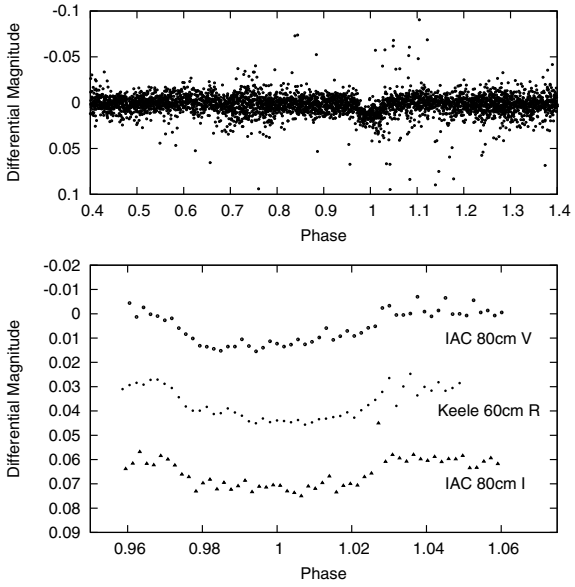

Figure 1. Light curves for 1SWASP J183431.62+353941.4 (WASP-3) obtained with SuperWASP-N (top panel), the IAC 80-cm telescope (*V* and *I*) and the Keele 60-cm telescope (*R*) as marked. The scatter in the post-eclipse *R*-band light curve was caused by deteriorating observing conditions. All the data (apart from that from SuperWASP-N) are averaged in 300-s bins, and are phased using the ephemeris derived in Section 3.2.1, $T_0 =$ BJD 245 4143.8504 and $P = 1.846\,834$ d.

Transit searches were carried out on this data set (Christian et al. 2006; Clarkson et al. 2007; Lister et al. 2007; Street et al. 2007) using the techniques outlined by Collier Cameron et al. (2006). 1SWASP J183431.62+353941.4, which we henceforth denote as WASP-3, was highlighted by Street et al. (2007) as a high-priority candidate worthy of further study. Fig. 1 (top panel) shows the original SuperWASP-N light curve, which comprises 3969 data points obtained over a 118 d period. In the original SuperWASP-N photometry 17 transits were observed with >50 per cent of a transit observed on 10 occasions. These data led to an ephemeris of $T_0 =$ BJD 245 3139.1748 and $P = 1.846\,800$ d which was used to plan further observations. The transit here has a depth of 0.013 mag and is 137 min in duration. Street et al. (2007) noted that assuming a main-sequence F5 host star, then this light curve would be consistent with a $1.3\,R_{\rm J}$ companion.

2.2 Higher precision photometric observations

WASP-3 was observed with the IAC 80-cm telescope as part of the Canarian Observatories' *International Time Programme* for 2007. The imaging camera on this telescope has an e2v Technology PLC CCD of 2148 × 2148 pixel giving a scale of 0.33 arcsec pixel^{-1} and a total field of view of 10.6 arcmin. Observations were taken during the transit of 2007 August 4, and consist of 327 images of 30- and 20-s integration in the *V* and *I* bands, respectively. This night was photometric but suffered from significant Saharan dust extinction, estimated to be ∼0.4 mag on La Palma from the SuperWASP-N real-time pipeline.

The images were bias subtracted with a stacked bias frame and flat-fielded with a stacked twilight flat-field image obtained in both filters using individual flats gathered over the course of the run. After the instrumental signatures were removed, source detection and aperture photometry were performed on all science frames using the CASU catalogue extraction software (Irwin & Lewis 2001). We chose an aperture size matched to the typical seeing (5 pixels, 1.5 arcsec) and selected five non-variable comparison stars in the field of WASP-3 to use in deriving the differential photometry. Of these comparison stars two were less than a magnitude, and the rest within 3 mag, of WASP-3's brightness. For each exposure, we summed the fluxes of the five comparison stars and divided by the flux of the target star to derive the differential magnitude of the target. The resulting *V*- and *I*-band light curves (Fig. 1) of WASP-3 have a precision of ∼4 mmag.

Further observations of WASP-3 were made with the Keele University Observatory 60-cm Thornton Reflector on 2007 September 10. This telescope is equipped with a 765 × 510 pixel Santa Barbara Instrument Group (SBIG) ST7 CCD at the f/4.5 Newtonian focus, giving a 0.68 arcsec pixel^{-1} resolution and a 8.63× 5.75 arcmin^2 field of view. During most of the period the weather was photometric except post egress where some cloud appeared. Altogether 644 × 20-s observations in the *R* band were obtained. After applying corrections for bias, dark current and flat-fielding in the usual way, aperture photometry on the two brightest comparisons were performed using the commercial software AIP4WIN (Berry & Burnell 2005).

Tracking errors and spurious electronic noise mean that systematic noise is introduced into the system at an estimated level of 2 mmag with periodicities of 2 (worm error) and ∼20 min (presently of unknown origin). No corrections have been applied for this effect.

2.3 OHP 1.9 m and SOPHIE

WASP-3 was observed with the Observatoire de Haute-Provence's 1.93-m telescope and the SOPHIE spectrograph (Bouchy et al. 2006), over the eight nights 2007 July 2–5 and August 27–30; a total of seven usable spectra were acquired. SOPHIE is an environmentally stabilized spectrograph designed to give long-term stability at the level of a few m s^{-1}. We used the instrument in its high efficiency mode, acquiring simultaneous star and sky spectra through separate fibres with a resolution of $R = 40\,000$. Thorium–argon calibration images were taken at the start and end of each night, and at 2- to 3-h intervals throughout the night. The RV drift never exceeded 2–3 m s^{-1}, even on a night-to-night basis.

Conditions during both runs varied from photometric to cloudy, but all nights were affected by strong moonlight. As WASP-3 has magnitude $V \sim 10.5$, integrations of 900 s give a peak signal-to-noise ratio (S/N) per resolution element of around 40–50. The Two Micron All Sky Survey (2MASS) colours ($J - H = 0.196$, $J - K = 0.242$) and reduced proper motion, RPM(J) = 1.14, for WASP-3 suggest a spectral type of about F7-8V, hence we cross-correlated the spectra against a G2V template provided by the SOPHIE control and reduction software (the control software offers a choice of several numerical cross-correlation masks, F0, G2, K0, K5 and M4, sampled at a resolution of 110 000). Experience has shown that the difference in spectral types between WASP-3 and the template do not measurably affect the derived velocities.

In all spectra the cross-correlation functions (CCFs) were contaminated by the strong moonlight. We corrected them by using the CCF of the spectrum in the sky fibre from the background light (mostly the Moon). We then scaled both CCFs by the difference of efficiency between the two fibres. Finally we subtracted the corresponding CCF of the background light from the star fibre, and fitted the resulting function by a Gaussian. The parameters obtained allow us to compute the photon noise uncertainty of the corrected RV measurement ($\sigma_{\rm RV}$), using the relation detailed in Collier Cameron et al. (2007a):

$$\sigma_{\rm RV} = 1.7\sqrt{(\rm FWHM)}/(\rm S/N \times Contrast).$$

Overall our RV measurements have an average photon noise uncertainty of 14 m s^{-1}. As our RV measurements are not photon noise limited, we quadratically added an RV component to those uncertainties of about 10 m s^{-1} (more details in Section 3.2.1). The log of the spectroscopic observations and barycentric RV is given in Table 1.

Table 1. Journal of RV measurements of WASP-3. The 1SWASP identifiers give the J2000 stellar coordinates of the photometric apertures; the USNO-B1.0 number denotes the star for which the RV measurements were secured. The quoted uncertainties in the RV errors include components due to photon noise (Section 2.3) and 10 m s^{-1} of jitter (Section 3.2.1) added in quadrature. The fourth and fifth columns give the FWHM of the CCF dip, and the contrast of the dip as a fraction of the weighted mean continuum level. The S/N at 550 nm is given in column 6.

BJD	$t_{\rm exp}$ (s)	$V_{\rm r}$ (km s^{-1})	FWHM (km s^{-1})	Contrast (per cent)	S/N	Observation conditions
1SWASP J183431.62+353941.4: USNO-B1.0 1256−0285133 = GSC 02636−00195 = WASP-3						
245 4286.5225	900	−5.751 ± 0.018	20.5	11.7	44	Photometric
245 4287.4563	900	−5.254 ± 0.020	19.8	11.8	37	Cloudy and moonlit
245 4289.3662	900	−5.259 ± 0.018	19.9	11.8	43	Photometric and moonlit
245 4340.3251	1800	−5.648 ± 0.013	19.7	12.2	75	Moonlit
245 4341.3989	900	−5.406 ± 0.015	19.7	12.1	53	Moonlit
245 4342.3198	900	−5.544 ± 0.019	19.8	12.0	39	Cloudy and moonlit
245 4343.4825	2100	−5.638 ± 0.013	19.8	12.2	75	Cloudy and moonlit

3 RESULTS AND ANALYSES

3.1 Stellar parameters

The SOPHIE spectra are individually of modest S/N, but when summed together they are suitable for a preliminary photospheric analysis of WASP-3. However, from experience we have found that the SOPHIE standard pipeline reduction does not fully remove the scattered light component within the spectrograph. While this does not affect RVs significantly, it can none the less have subtle effects on absorption line depths, adversely affecting the derived spectral synthesis parameters.

Therefore we carefully rereduced the first three raw images (these data being least affected by moonlight) taken over 2007 July 2–5 with the REDUCE echelle data reduction package (Piskunov & Valenti 2002), paying careful attention to the issue of scattered light.

Following our analysis of WASP-1 (Stempels et al. 2007), we employed the methodology of Valenti & Fischer (2005), using the same tools, techniques and model atmosphere grid. We used the IDL-based software Spectroscopy Made Easy (SME) (Valenti & Piskunov 1996) to calculate and fit synthetic spectra using a multidimensional least-squares approach.

We concentrated our analysis on five regions in the spectrum (see Fig. 2). These regions allow us to constrain the stellar effective temperature, $T_{\rm eff}$ (through the broad wings of Hα and, to a lesser extent, Na I D 5890 Å), gravity log g (through Mg I*b* 5175 Å and Na I D 5890 Å) and the metallicity [M/H] (through the weak photospheric absorption lines in the 6000–6200 Å region). We also measured the abundance of lithium from the Li I 6708 Å line. The combined spectrum is not of sufficient quality to perform a detailed abundance analysis. The parameters we obtained from this analysis are listed in Table 2, and a comparison between observed and synthesized profiles is shown in Fig. 2. In addition to the spectrum analysis, we also used Tycho ($B = 11.11$, $V = 10.68$) and 2MASS photometry to estimate the effective temperature using the infrared flux method (Blackwell & Shallis 1977). This gives $T_{\rm eff} = 6200 \pm 300$ K, which is in close agreement with that obtained from the spectroscopic analysis. The Tycho and 2MASS colours ($V - K = 1.32$, $V - H = 0.2$) also suggest a spectral type of F7-8V (Collier Cameron et al. 2006; Street et al. 2007).

In our spectra the Li I λ6708 Å line is weak, but still measurable, and we derive a lithium abundance of log n(Li) = (Li/H) + 12 = 2.0–2.5. However, at this stellar temperature it is thought that stellar age does not correlate well with lithium abundance (Sestito & Randich 2005), so we have examined the evolutionary tracks for low- and intermediate-mass stars presented by Girardi et al. (2000) using a maximum likelihood fitting routine. Using our derived stellar parameters we find the stellar mass $M_* = 1.24 \pm 0.08$ with an age of 0.7–3.5 Gyr.

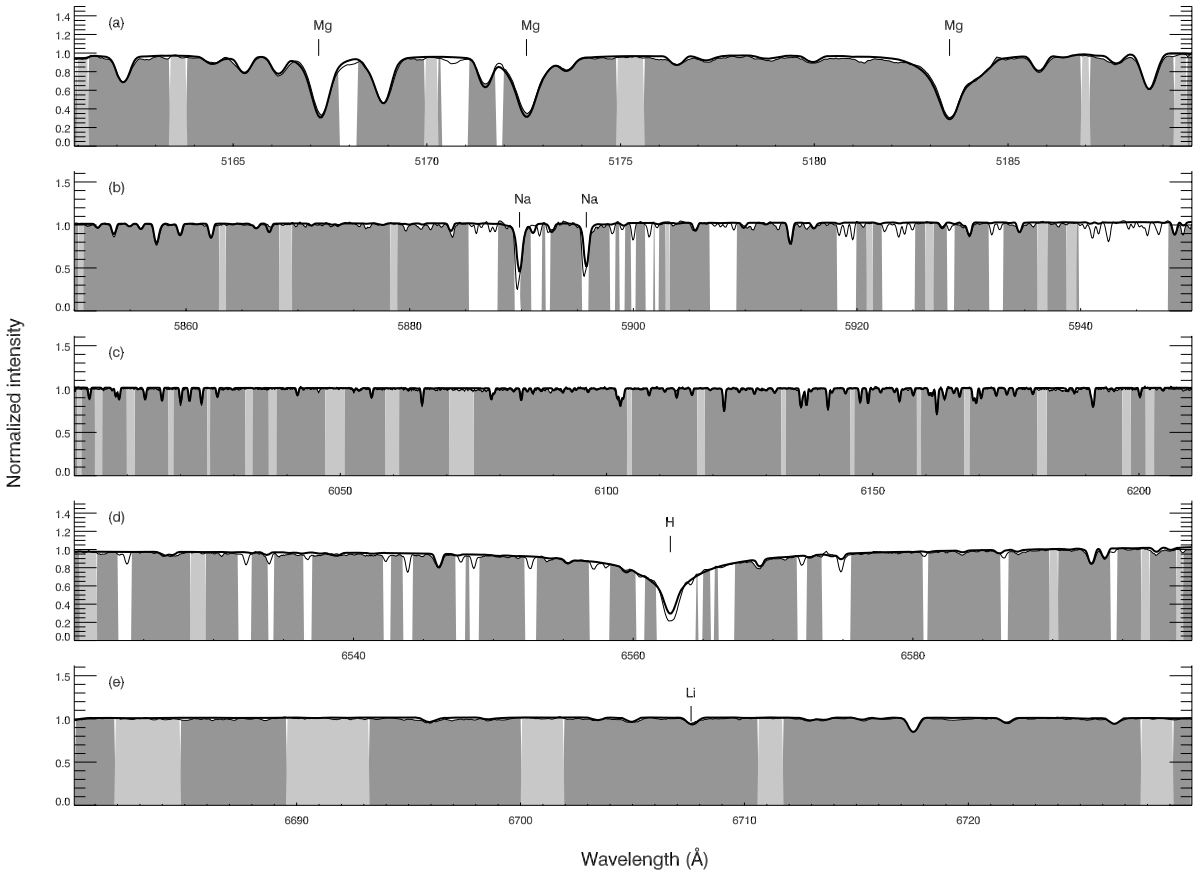

Figure 2. A comparison between the synthetic spectrum from SME (thick, black line) with the observed SOPHIE spectrum (thin, grey line). In some regions the agreement between the model and observations is excellent, making the observed spectrum difficult to see. The synthetic spectrum was calculated using the parameters from Table 2. The white regions are excluded from the spectral analysis, mainly because of the presence of telluric absorption. Light shaded regions were used to determine the continuum level, and the remaining dark shaded regions to determine the stellar atmospheric parameters. All five spectral sections were used simultaneously. The five sections contain (a) the Mg I*b* triplet near 5175 Å; (b) the Na I D doublet (excluding the line cores) near 5890 Å; (c) a large region with well-isolated lines of a wide range of metals; (d) the wings of the Hα line at 6563 Å and (e) the Li I line at 6707 Å.

Table 2. Parameters for WASP-3 as derived from the SME analysis of the SOPHIE spectroscopy.

Parameter	WASP-3
$T_{\rm eff}$	6400 ± 100 K
$\log g$	4.25 ± 0.05
[M/H]	0.00 ± 0.20
$v \sin i$	13.4 ± 1.5 km s^{-1}
$v_{\rm rad}$	-5.490 ± 0.007 km s^{-1}

3.2 The reflex motion of the host star

3.2.1 Markov Chain Monte Carlo analysis

The SOPHIE RV data measurements are plotted in Fig. 3 together with the best-fitting global fit to the SuperWASP-N, IAC 80-cm and Keele transit photometry. Since the timing of the transits and the RV solution both provide information about the orbit, we modelled the transit photometry and the reflex motion of the host star simultaneously.

The model of the primary star's RV orbit is parametrized in the usual way by the primary's RV amplitude K_1, the centre-of-mass velocity γ, the orbital eccentricity e and the longitude ω of periastron.

The transit profile was modelled using the small-planet approximation of Mandel & Agol (2002), with the four-coefficient nonlinear limb-darkening model of Claret (2000). We used R-band limb-darkening coefficients for the SuperWASP-N data, whose unfiltered wavelength response is centred near the R band, and for the Keele R-band data. We used the appropriate V- and I-band limb-darkening coefficients for the IAC 80-cm photometry. The transit model was characterized by the epoch T_0 of mid-transit, the orbital period P, the duration $t_{\rm T}$ from first to fourth contact, the squared ratio $\Delta F = (R_{\rm p}/R_*)^2$ of the planet radius $R_{\rm p}$ to the stellar radius R_*, and the impact parameter $b = a(1 - e\cos\ E_{\rm T})\cos\ i/R_*$ of the planet's trajectory across the face of the host star. Here a is the orbital semimajor axis, $E_{\rm T}$ is the eccentric anomaly at the epoch of transit and i is the orbital inclination. The ratio of the stellar radius to the orbital separation is then given approximately (or exactly for a circular orbit) by

$$\frac{R_*}{a} = \frac{t_{\rm T}}{P}\frac{\pi}{(1+\sqrt{\Delta F})^2 - b^2}$$

(Collier Cameron et al. 2007b). The orbital semimajor axis is derived from the orbital period and the stellar mass M_* via Kepler's third law. The value of the stellar mass $M_* = 1.24 \pm 0.08$ M$_\odot$ is taken from the isochrone fit described in Section 3.1 above.

The set of nine parameters $\{T_0, P, t_{\rm T}, \Delta F, b, M_*, K_1, e, \omega\}$ thus defines both the transit light curve and the form of the reflex velocity variation. We compute the photometric zero-point offset Δm of the observed magnitudes m_j from the model μ_j derived from a given set of parameters:

$$\Delta m = \frac{\sum_j (m_j - \mu_j) w_j}{\sum_j w_j}.$$

The weights w_j are the inverse variances $1/\sigma_j^2$ of the individual observations. Similarly, we compute the RV γ of the system's centre of mass as the inverse-variance-weighted mean offset between the observed RVs w_k and the model values v_k for the current model parameters:

$$\gamma = \frac{\sum_k (v_k - v_k) w_k}{\sum_k w_k}.$$

We quantify the goodness of fit to the data by the combined χ^2 statistic for the combined photometric and RV data:

$$\chi^2 = \sum_{j=1}^{N_{\rm p}} \frac{(m_j - \mu_j - \Delta m)^2}{\sigma_j^2} + \sum_{k=1}^{N_v} \frac{(v_k - v_k - \gamma)^2}{\sigma_k^2}.$$

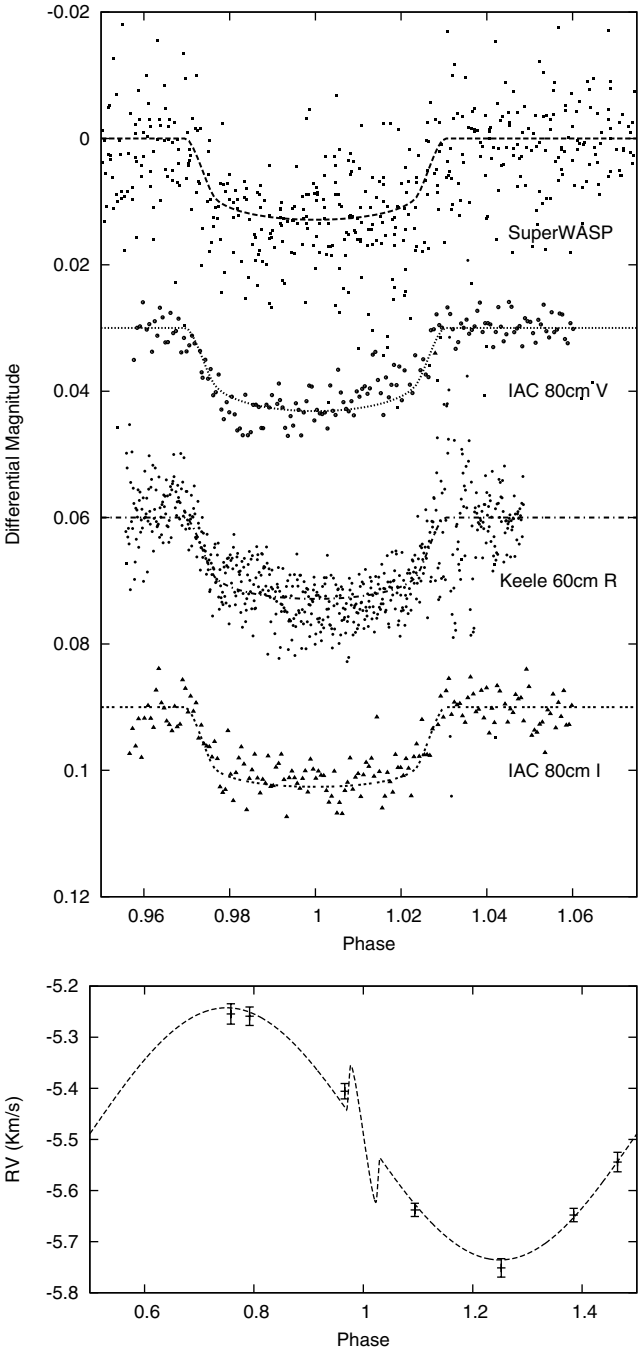

Figure 3. Simultaneous MCMC solution to combined SuperWASP-N, IAC 80-sm V, I and Keele R photometry. The orbital solution is assumed to be circular. The lower panel is the MCMC solution to the RV data. The model here also shows the Rossiter–McLaughlin effect which is predicted to be significant in this system given the host's $vsini = 13.40$ km s^{-1}.

Markov Chain Monte Carlo (MCMC) analysis has recently become established as an efficient and reliable method for establishing both photometric (Holman et al. 2006; Burke et al. 2007) and orbital (Ford 2006; Gregory 2007) parameters of close-orbiting giant exoplanets. We determined the photometric and orbital parameters of the WASP-3 system using the MCMC algorithm described in detail by Collier Cameron et al. (2007b), to which we refer the reader for most details of the implementation. The initial photometric solution for the SuperWASP-N transit profiles is established by our transit-search algorithm (Collier Cameron et al. 2006). The initial RV solution is an inverse-variance-weighted linear least-squares fit assuming a circular orbit. In both cases, the initial fits also yield good estimates of the parameter uncertainties. The stellar mass is initialized at the value $M_0 = 1.24$ M$_\odot$ estimated from isochrone fitting.

At each step in the algorithm, each of the nine proposal parameters is perturbed by a small random amount such that

$$T_{0,i} = T_{0,i-1} + \sigma_{T_0} G(0,1) f$$

and similarly for the other eight parameters. Here $G(0, 1)$ is a random Gaussian deviate with mean zero and unit standard deviation. The adaptive step-size controller f is initially set to 0.5, and evolves as the calculation progresses, ensuring that roughly 25 per cent of proposal sets are accepted.

The prior probability distributions for all nine parameters are treated as being uniform. The parameters P, t_T, ΔF, M_* and K_1 are required to be positive. The impact parameter and eccentricity are restricted to the ranges $0 < b < 1$ and $0 < e < 1$, while the longitude of periastron is restricted to the range $-\pi < \omega < \pi$. The decision on whether or not to accept a set of proposal parameters is made via the Metropolis–Hastings algorithm using the logarithmic likelihood functional

$$Q_i = \chi_i^2 + \frac{(M_{*,i} - M_0)^2}{\sigma_M^2} + \frac{(\log g_{*,i} - \log g_*)^2}{\sigma_{\log g}^2},$$

where $\log g_{*,i}$ is computed directly from the mass $M_{*,i}$ and radius $R_{*,i}$. This imposes a Gaussian prior on the stellar mass, and indirectly on the radius. The prior forces the stellar mass to be close to the initial estimate M_0 with an assumed uncertainty $\sigma_M = 0.1 M_0$. The prior on $\log g_*$ ensures consistency with the spectroscopically measured value $\log g_* = 4.25 \pm 0.05$, and thus helps to reduce the uncertainty in the stellar radius if the impact parameter is not strongly constrained by the photometry.

If a new set of proposal parameters yields $Q_i < Q_{i-1}$, the fit to the data is improved and the proposal is accepted. If $Q_i > Q_{i-1}$, the parameter set is accepted with probability $\exp[(Q_{i-1} - Q_i)/2]$. We find that the solution converges within a few hundred steps to a stable, optimal solution. After this initial 'burn-ini' phase, we rescale the photometric error bars so that the contribution of each photometric data set to χ^2 is equal to the associated number of degrees of freedom. The uncertainty in the RV measurements combines the photon noise error estimate given in Section 2.3 with unknown additional variances including stellar jitter and systematic errors arising from thermal drifts and the background moonlight subtraction. We estimated the additional variance arising from these effects by requiring that the χ^2 of the fit to the spectroscopic data be equal to the number of degrees of freedom. The effect of this additional variance is equivalent to adding RV 'jitter' with amplitude 10 m s^{-1} in quadrature with the photon noise uncertainties, giving the values listed in Table 1. We then run the algorithm for a few hundred further steps and derive revised parameter uncertainties from the standard deviations of their respective Markov Chains. This optimizes the step length used in generating new sets of proposal parameters. Finally the algorithm is allowed to run for 10^5 steps in order to map out the joint posterior probability distribution of the nine proposal parameters.

Table 3. WASP-3 system parameters and 1σ error limits derived from MCMC analysis. Here the γ velocity is treated as a zero-point correction obtained by subtracting the model RV curve at each MCMC step and then taking the inverse variance weighted mean of the residuals.

Parameter	Symbol	Value	Units
Transit epoch (BJD)	T_0	$2454143.8503^{+0.0004}_{-0.0003}$	d
Orbital period	P	$1.846\,834^{+0.000\,002}_{-0.000\,002}$	d
Planet/star area ratio	$(R_\mathrm{p}/R_\mathrm{s})^2$	$0.0106^{+0.0002}_{-0.0004}$	
Transit duration	t_T	$0.1110^{+0.0009}_{-0.0018}$	d
Impact parameter	b	$0.505^{+0.051}_{-0.166}$	R_*
Stellar reflex velocity	K_1	$0.2512^{+0.0079}_{-0.0108}$	km s^{-1}
Centre-of-mass velocity	γ	$-5.4887^{+0.0013}_{-0.0018}$	km s^{-1}
Orbital semimajor axis	a	$0.0317^{+0.0005}_{-0.0010}$	au
Orbital inclination	I	$84.4^{+2.1}_{-0.8}$	degrees
Stellar mass	M_*	$1.24^{+0.06}_{-0.11}$	M$_\odot$
Stellar radius	R_*	$1.31^{+0.05}_{-0.12}$	R$_\odot$
Stellar surface gravity	$\log g_*$	$4.30^{+0.07}_{-0.03}$	(CGS)
Stellar density	ρ_*	$0.55^{+0.15}_{-0.05}$	$\rho_\odot$
Planet radius	R_p	$1.31^{+0.07}_{-0.14}$	R_J
Planet mass	M_p	$1.76^{+0.08}_{-0.14}$	M_J
Planetary surface gravity	$\log g_\mathrm{p}$	$3.37^{+0.09}_{-0.04}$	(CGS)
Planet density	ρ_p	$0.78^{+0.28}_{-0.09}$	ρ_J
Planet temperature ($A = 0$)	T_eql	1960^{+33}_{-76}	K

We find that for WASP-3 the nine proposal parameters show only weak mutual correlations. The correlation lengths (Tegmark et al. 2004) of the Markov Chains for individual parameters are typically 10–20 steps, so the final production run yielded approximately 10^4 statistically independent parameter sets. In the initial runs we allowed all nine parameters to float, and arrived at a solution with eccentricity $e = 0.05 \pm 0.05$. Since this is statistically indistinguishable from the circular orbit expected for a planet with such a short period, the remaining eight parameters were fitted assuming $e = 0$.

The values of the parameters at the optimal solution are given, together with their associated 1σ (68.3 per cent) confidence intervals, in Table 3. These results are consistent with those derived from the spectral analysis presented earlier.

While it may be expected that the intrinsic accuracy and noise in the SuperWASP-N data may lead to better solutions if omitted from the final fits, the use of inverse-variance weighting ensures that these data do not significantly degrade the final radius determination (the follow-up photometry alone gives $R_\mathrm{p} \sim 1.28 \pm 0.10 R_\mathrm{J}$). Furthermore, their inclusion is in fact essential for accurate period determination. Note that the errors on the individual photometric data sets were rescaled during the MCMC burn-in phase to ensure that the post-fit χ^2 for each subset was equal to the number of degrees of freedom.

By adopting a fixed orbital period we have solved the individual IAC 80-cm V-, I-band light curves, and Keele 60-cm R-band light

Table 4. Dependence of stellar and planetary parameters on $\log g_*$. $\chi^2_{\rm ph}$ refers to the fitting of the photometric light curves with $\log g = 0.01$.

$\log g$ (CGS)	$\chi^2_{\rm ph}$	b	M_* ($M_\odot$)	R_* ($R_\odot$)	$R_{\rm p}$ ($R_{\rm J}$)	$\rho_{\rm p}$ ($\rho_{\rm J}$)
4.05	4492.6	0.76	1.14	1.64	1.75	0.31
4.15	4478.6	0.68	1.18	1.50	1.55	0.46
4.25	4470.9	0.58	1.23	1.37	1.39	0.65
4.35	4468.1	0.38	1.22	1.22	1.20	1.00
4.45	4468.9	< 0.09	1.36	1.17	1.14	1.25
4.55	4491.1	< 0.05	1.60	1.20	1.16	1.32

curves. We find the $R_{\rm p} = 1.40^{+0.11}_{-0.13}$, $1.26^{+0.11}_{-0.10}$, $1.46^{+0.11}_{-0.12}$, respectively. These results are consistent at the 1σ level with those obtained from the combined SuperWASP and follow-up photometry. Within the accuracy of the photometry this would seem to rule out a blended system (Tingley 2004; O'Donovan et al. 2006).

We explored the relationship between the stellar surface gravity and the impact parameter of the transit by repeating the fit for a sequence of values of $\log g$, with an artificially restricted $\sigma_{\log g} = 0.01$. The results are given in Table 4. The best formal fit to the photometry, $\chi^2_{\rm ph}$, is obtained for stellar surface gravities in the range $4.35 < \log g < 4.45$. In this range, however, the stellar radius is unphysically low in relation to the stellar mass. At the spectroscopically determined $\log g = 4.25$, the photometric χ^2 is only marginally degraded. At still lower values of $\log g$, the impact parameter increases to the point where the duration of transit ingress and egress cannot be fitted satisfactorily. Moreover, the radii of the star and the planet become implausibly inflated. We conclude that the stellar surface gravity must lie in the range $4.25 < \log g < 4.35$, and the impact parameter in the range $0.4 < b < 0.6$. The limits on these parameters derived from the full posterior probability distribution, as listed in Table 3, are consistent with this conclusion.

3.2.2 Line-bisector analysis

It is well known that faint binaries contaminating the photometric aperture, or even stellar activity, can influence absorption line shape and can, in certain circumstances, mimic or confuse small RV motions. By noting the position of the line bisector of the CCF, asymmetries in the profile will become apparent. If these variations are due to blending we would expect variations in the bisector to be correlated with the orbital phase (Santos et al. 2002).

We measured the asymmetries of the CCF peaks using the line-bisector method as a function of RV (Gray 1988), as applied by Queloz et al. (2001). Fig. 4 demonstrates that periodic variations, indicative of line-of-sight binarity or activity are not apparent. Furthermore, the scatter in bisector velocities is substantially less than the measured orbital velocity amplitude, and is uncorrelated with orbital phase. Hence, while we cannot rule out some kinds of exotic systems, we are confident that the RV variations are genuinely due to the orbital motion of a low-mass object.

While a visual examination of the data shows little evidence of any correlation, the small sample size makes any quantitative analysis of low significance. None the less, a simple correlation analysis suggests a coefficient, $R = 0.11$ suggesting almost no relationship between the variables, hence confirming the visual inspection.

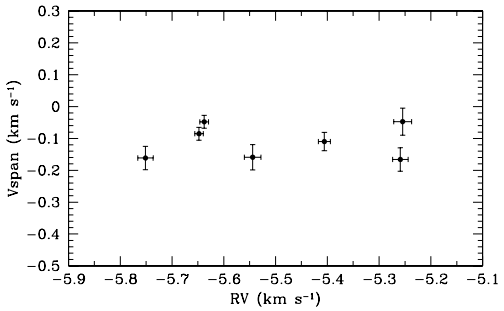

Figure 4. Analysis of line bisectors in WASP-3 shows the bisector velocity (vspan) does not correlate with stellar RV. This demonstrates that the CCF remains symmetric, and that the RV variations are not likely to be caused by line-of-site binarity or stellar activity. The offset from zero in the line bisector is probably caused by distortion of the CCF by the background (moonlight) correction.

3.3 Adaptive optics imaging

We further investigated the scenario of a triple system comprising a bright single star and a faint, blended eclipsing-binary system by performing high-resolution *H*-band imaging with the near-infrared camera INGRID, fed by the adaptive optics system NAOMI, on the 4.2-m William Herschel Telescope. An image taken in natural seeing of 0.8 arcsec with corrected full width at half-maximum (FWHM) of 0.2 arcsec shows no evidence for resolved companions to WASP-3. At this distance we estimate we would be able to detect companions 2–3 mag fainter than WASP-3, rising to ∼5 mag at 1 arcsec. These brightness estimates correspond to the combined light output of a ∼K0 star at 0.2 and a late K/M0 star at 1 arcsec distance. Whilst these companions would all lie within the aperture of the SOPHIE observations, the quality of the spectra is not sufficient to discriminate even the brightest of these blends. Assuming an F7-8V spectral type ($M_v \sim 3.8$) for WASP-3 would imply a distance of ∼220 pc, hence these observations constrain any potential associated bright eclipsing binary companion to lie within ∼45 au of the host. Of course, if any potential blend is not actually associated with WASP-3 (i.e. a line of sight blend) then we have no constraint on its distance and hence its nature.

4 DISCUSSION

In this study we have found WASP-3b to be a transiting gas-giant exoplanet with mass $1.76^{+0.08}_{-0.14}\ M_{\rm J}$ and radius $1.31^{+0.07}_{-0.14}\ R_{\rm J}$. Its host star, WASP-3, has a photospheric temperature of 6400 ± 100 K and $\log g = 4.25 \pm 0.05$, consistent with its F7-8V spectral type derived from 2MASS photometry. This places WASP-3b amongst the most massive of known transiting exoplanets (Fig. 5). Given the host's relatively large rotational velocity and the large radius of the planet we would expect a significant amplitude for Rossiter–McLaughlin effect (the model is included in Fig. 3).

Sozzetti et al. (2007) demonstrate a correlation of planet radius with host mass for 14 confirmed transiting exoplanets, and a correlation of planet mass with orbital period for the same sample (first noted by Mazeh, Zucker & Pont (2005)). Fig. 6 shows these relationships updated, while in Fig. 7 we also update the apparent correlation of surface gravity with orbital period noted by Southworth, Wheatley & Sams (2007). Despite the additional objects the R_P versus M_* correlation remains weak (even ignoring the two most massive objects HD17156b and HD147506b). For both the M_P versus P and g versus P we contend that these relationships arise partly through

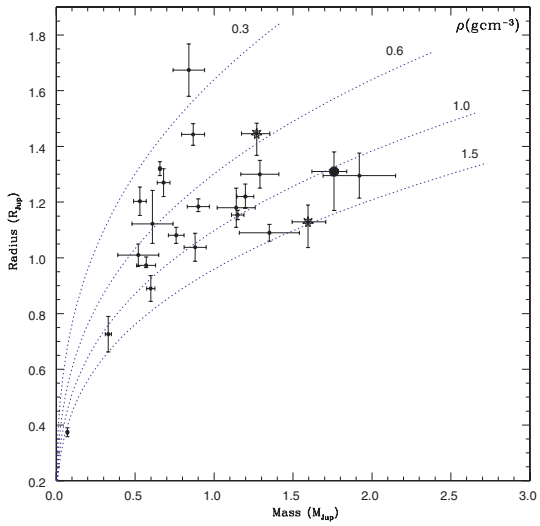

Figure 5. The known confirmed transiting exoplanets plotted in the mass–radius plane. Isodensity contours are plotted in CGS units. For clarity of scale we have not plotted HD17156 (mass 3.12 M_J, radius 1.15 R_J) or the extremely high-density object HD147506b (mass 8.04 M_J, radius 0.98 R_J). WASP-3b is marked as a filled circle (data from http://obswww.unige.ch∼pont/TRANSITS.htm and references therein). Two newly discovered WASP planets, WASP-4b (mass 1.27 M_J, radius 1.45,R_J) (Wilson et al. 2008) and WASP-5b (mass 1.13 M_J, radius 1.60, R_J) (Anderson et al. 2008) are also shown.

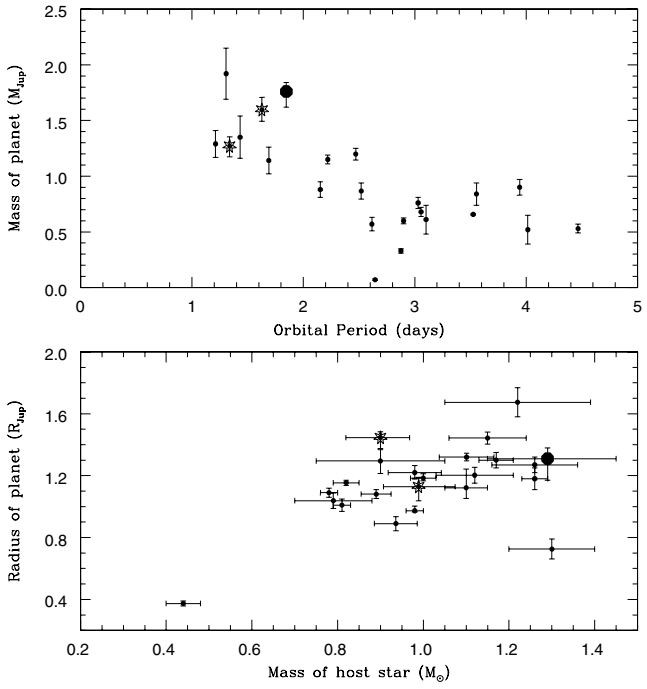

Figure 6. Modified version of fig. 5 from Sozzetti et al. (2007), incorporating a further seven newly discovered systems (data from http://obswww.unige.ch/pont/TRANSITS.htm and references therein, but again excluding HD17156b and HD147506b). In each case WASP-3b is marked by the filled circle. Two newly discovered WASP planets, WASP-4b ($P = 1.338$ d, host mass 0.90 $M_\odot$) (Wilson et al. 2008) and WASP-5b ($P = 1.628$ d, host mass 0.99 $M_\odot$) (Anderson et al. 2008) are also shown.

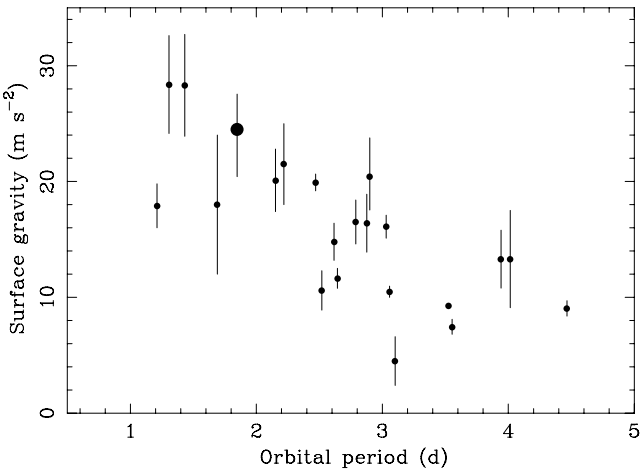

Figure 7. The correlation of planetary surface gravity with orbital period for the 22 shortest period transiting planets (updated version of fig. 2 from Southworth et al. (2007)).

observational selection and partly through the effects of the intense radiation fields that these planets are experiencing. We believe the absence of high-gravity/high-mass bodies at longer periods is primarily a detection effect, while the absence of low-gravity/low-mass planets at short period could indeed be caused by rapid evaporation.

The closeness of the orbit and the large radius and high effective temperature of the host star combine to make WASP-3b one of the most strongly irradiated, and hence one of the hottest of the known exoplanets, second only to OGLE-TR-56b and comparable to OGLE-TR-132. This raises the possibility that the atmosphere may be hot enough for TiO and VO to remain in the gas phase above the temperature minimum, creating a hot, strongly absorbing stratosphere (Fortney et al. 2006). This would give an anomalously high infrared brightness temperature, as Harrington et al. (2007) inferred from *SPITZER/IRAC* secondary-eclipse photometry of HD149026b at 8 μm. Being much closer and brighter than any of the OGLE host stars, WASP-3b is thus an excellent candidate for future observational tests of the hot-stratosphere hypothesis.

ACKNOWLEDGMENTS

The WASP Consortium consists of astronomers primarily from the Universities of Cambridge (Wide Field Astronomy Unit), Keele, Leicester, The Open University, Queen's University Belfast and St Andrews, the Isaac Newton Group (La Palma), the Instituto de Astrofísica de Canarias (Tenerife) and the South African Astronomical Observatory. The SuperWASP-N and WASP-S Cameras were constructed and operated with funds made available from Consortium Universities and the UK's Science and Technology Facilities Council (formerly PPARC). We extend our thanks to the Director and staff of the Isaac Newton Group of Telescopes and the South African Astronomical Observatory for their support of SuperWASP-N and WASP-S operations, and the Director and staff of the Observatoire de Haute-Provence for their support of the SOPHIE spectrograph. FPK would like to acknowledge AWE for the award of a William Penney Fellowship. We would also like to thank an anonymous referee for their careful and thorough reading of the original manuscript and their thought provoking comments.

REFERENCES

Anderson D. et al., 2008, MNRAS, submitted
Arras P., Bildsten L., 2006, ApJ, 650, 394
Bakos G. A., Noyes R. W., Kovács G., Stanek K. Z., Sasselov D. D., Domsa I., 2004, PASP, 116, 266
Berry R., Burnell J., 2005, The Handbook of Astronomical Image Processing, 2nd edn. Willmann-Bell, Richmond, VA
Blackwell D. E., Shallis M. J., 1977, MNRAS, 180, 177
Bouchy F., The Sophie Team, 2006, in Arnold L., Bouchy F., Moutou C., eds, Tenth Anniversary of 51 Peg-b: Status of and Prospects for Hot Jupiter Studies. Frontier Goup, Paris, p. 319
Burke C. J. et al., 2007, ApJ, 671, 2115
Burrows A., Hubeny I., Budaj J., Hubbard W. B., 2007, ApJ, 661, 502
Charbonneau D., Brown T. M., Latham D. W., Mayor M., 2000, ApJ, 529, L45
Christian D. et al., 2006, MNRAS, 372, 1117
Claret A., 2000, A&A, 363, 1081
Clarkson W. et al., 2007, MNRAS, 381, 851
Collier Cameron A. et al., 2006, MNRAS, 373, 799
Collier Cameron A. et al., 2007a, MNRAS, 375, 951
Collier Cameron A. et al., 2007b, MNRAS, 380, 1230
Dunham E. W., Mandushev G. I., Taylor B. W., Oetiker B., 2004, PASP, 116, 1072
Ford E. B., 2006, ApJ, 642, 505
Fortney J. J., Saumon D., Marley M. S., Lodders K., Freedman R. S., 2006, ApJ, 642, 495
Fortney J. J., Marley M. S., Barnes J. W., 2007, ApJ, 659, 1661
Gaudi B. S., 2005, ApJ, 628, L73
Gaudi B. S., Seager S., Mallen-Ornelas G., 2005, ApJ, 623, 472
Girardi L., Bressan A., Bertelli G., Chiosi C., 2000, A&AS, 141, 371
Gregory P. C., 2007, MNRAS, 374, 1321
Gray D. F., 1988, Lectures on Spectral-line Analysis: F, G, and K Stars. The Publisher, Arva, Ontario
Gu P., Bodenheimer P. H., Lin D. N. C., 2004, ApJ, 608, 1076
Guillot T., Santos N. C., Pont F., Iro N., Melo C., Ribas I., 2006, A&A, 453, L21
Harrington J., Luszcz S., Seager S., Deming D., Richardson L. J., 2007, Nat, 447, 691
Henry G. W., Marcy G. W., Butler R. P., Vogt S. S., 2000, ApJ, 529, L41
Holman M. J. et al., 2006, ApJ, 652, 1715
Horne K. D., 2003, in Deming D., Seager S., eds, ASP Conf. Ser. Vol. 294, Scientific Frontiers of Exoplanet Research. Astron. Soc. Pac., San Francisco, p. 361
Irwin M., Lewis J., 2001, New Astron. Rev., 45, 105
Lister T. et al., 2007, MNRAS, 379, 647
Mandel K., Agol E., 2002, ApJ, 580, L171
Mayor M., Queloz D., 1995, Nat, 378, 355
Mazeh T., Zucker S., Pont F., 2005, MNRAS, 356, 955
McCullough P. R. et al., 2006, ApJ, 648, 1228
O'Donovan F. T. et al., 2006, ApJ, 644, 1237
Piskunov N. E., Valenti J. A., 2002, A&A, 385, 1095
Pollacco D. et al., 2006, PASP, 118, 1407
Pont F., Zucker S., Queloz D., 2006, MNRAS, 373, 231
Queloz D. et al., 2001, A&A, 379, 279
Santos N. C. et al., 2002, A&A, 392, 215
Sato B. et al., 2005, ApJ, 633, 465
Sestito P., Randich S., 2005, A&A, 442, 615
Smith A. et al., 2006, MNRAS, 373, 1151
Southworth J., Wheatley P. J., Sams G., 2007, MNRAS, 379, L11
Sozzetti A., Torres G., Charbonneau D., Latham D. W., Holman M. J., Winn J. N., Laird J. B., O'Donavan F. T., 2007, ApJ, 664, 1190
Street R. A. et al., 2007, MNRAS, 379, 816
Stempels H. C., Collier Cameron A., Hebb L., Smalley B., Frandsen S., 2007, MNRAS, 379, 773
Tegmark M. et al., 2004, Phys. Rev. D, 69, 103501
Tingley B., 2004, A&A, 425, 1125
Udalski A. et al., 2002, Acta Astron., 52, 1
Valenti J. A., Fischer D., 2005, ApJS, 159, 141
Valenti J. A., Piskunov N., 1996, A&AS, 118, 595
Wilson D. et al., 2008, ApJ, preprint (arXiv:0801.1509)

This paper has been typeset from a TEX/LATEX file prepared by the author.